

Understanding Challenges of Cathode Materials for Sodium-Ion Batteries using Synchrotron-Based X-Ray Absorption Spectroscopy

Mingzhe Chen,^[a] Shu-Lei Chou,*^[a] and Shi-Xue Dou^[a]

An in-depth understanding of the electrochemical behavior of cathode materials in a complex chemical environment is critical for the development of state-of-the-art sodium-ion batteries. Advanced synchrotron-based characterization is a powerful tool for collecting valuable information on complicated reaction mechanisms. X-ray absorption spectroscopy can be used to precisely monitor the valence state and corresponding changes during cycling of various elements. Information on the local structure, such as coordination number and bond information

can also be extracted from the fitting data in Fourier transform extended X-ray absorption fine structure. In this review, we summarize findings on state-of-the-art cathode materials using ex-situ/in-situ X-ray absorption spectroscopy to probe fundamental discoveries on sodium-ion battery systems and what important and valuable results have been obtained. Further possible improvements and practical operating advice are also discussed in detail.

1. Introduction

In rechargeable battery technology, we have witnessed the rapid development of various energy storage intermediates from sustainable and renewable sources in the past few decades, due to their scale flexibility, economical maintenance, and high energy transfer efficiency compared to other energy storage facilities.^[1,2] As the most promising rechargeable battery system, lithium-ion batteries (LIBs) have experienced successful commercialization in the portable devices and electric vehicles (EVs) in recent years. The limited and unevenly distributed nature of lithium sources remains the main obstacle, however, to the urgent need for low-cost batteries in the future. In this scenario, sodium-ion batteries (SIBs) have been of great interest in very recent years for large-scale energy storage facilities, since sodium resources are nearly inexhaustible.^[3] Li and Na fall under Group I alkali metals in the periodic table, and they share similar chemical properties in various chemical circumstances. The use of Na^+ as the charge carrier has several shortcomings compared to Li^+ , however, since the radius of Na^+ (1.02 Å) is larger than that of Li^+ (0.76 Å), which will result in large volume shrinkage as well as inferior cycling performance.^[4–6] To overcome these disadvantages preventing the real application of SIBs, great challenges, such as discovering more promising electrodes or achieving an in-depth understanding of the mechanisms, are inevitably encountered for both cathode and anode materials as well as suitable electrolytes.^[7,8]

Cathode materials mainly determine the overall energy density, lifespan, and tolerance of full SIBs. The parameters of

specific capacity, working potential, and volume change, as well as the individual crystal structure, are all critical factors for the ultimate electrochemical performance.^[9] There are three main types of cathode materials for SIBs: layered-/tunnel-structure sodium transition metal oxides; polyanion cathodes, including pyrophosphates, (fluoro)sulfates, and (fluoro)phosphates; and Prussian blue/white analogues and organic compounds.^[10–12] Most of the cathode materials operate by the de/intercalation reaction mechanism for sodium storage, so that monitoring and understanding these phase transitions, crystal structure variations, valence changes, and interfacial behavior of cathode materials are vitally important for improvement of the electrochemical properties of SIBs. The following are the major fundamental concerns for materials optimization: (1) the relationship between the crystal structure, local structure, and specific sodium storage behavior; (2) the origin of charge transfer, compensation and capacity; (3) the relationship between performance and reaction anisotropy as well as thermal dynamics and kinetics; and (4) interfacial behavior regarding the solid-electrolyte interphase (SEI) layer.^[11] Therefore, an in-depth understanding of these specific aspects relating to SIBs requires more advanced characterization techniques, especially high-energy synchrotron-based technologies (Figure 1).

Over the past few decades, remarkable achievements in synchrotron-based X-ray techniques have provided significant opportunities to investigate the working mechanisms of battery materials, especially cathode materials.^[8,13] When used in cooperation with other scattering, spectroscopy, and imaging techniques, integrated studies have been carried out to better understand the complicated issues for SIBs at multiple length scales. More importantly, high-resolution synchrotron X-ray sources can provide in-situ/operando examination with various beamlines to study their dynamic properties as well as time-dependent reaction processes. For the localized structure

[a] Dr. M. Chen, Dr. S.-L. Chou, Prof. S.-X. Dou
Institute for Superconducting and Electronic Materials
Australian Institute for Innovative Materials
University of Wollongong, Innovation Campus
Squires Way, North Wollongong NSW 2522, Australia
E-mail: shulei@uow.edu.au

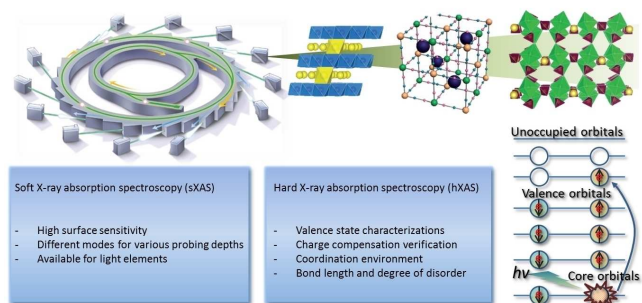


Figure 1. Introduction to applications of X-ray absorption spectroscopy on cathode materials of LIBs and representative capabilities of both soft and hard X-ray absorption spectroscopy.

changes and variation through multiple valence states, hard and soft X-ray absorption spectroscopy (hxAS/sxAS) can precisely monitor the valence state and corresponding changes during cycling of various elements (Figure 1). Meanwhile, local structure information, such as the coordination number and bond information can also be extracted from the fitting data in Fourier transform extended X-ray absorption fine structure measurements. These changes are essential and critical for achieving an in-depth understanding of cathode materials as both the valences and the chemical circumstances around adsorbed atoms are very sensitive but can offer valuable information during charge/discharge processes.^[14]

Considering the importance of advanced X-ray absorption spectroscopy (XAS) characterization techniques in sodium-ion battery studies, herein, we present a timely and concisely review of state-of-the-art studies of cathode materials based on synchrotron-based XAS technology. We aim to provide some basic guidance for researchers in the electrode field that can lead to a more comprehensive understanding and highlight the irreplaceable importance of advanced XAS techniques with some of the latest exciting findings. We also propose some emerging and promising research directions where the XAS technique can make significant contributions.



Mingzhe Chen received his Master's degree in 2015 from Sichuan University, China. He obtained his Ph. D. degree at the Institute for Superconducting and Electronic Materials, University of Wollongong under the supervision of Dr. Shu-Lei Chou and Prof. Shi-Xue Dou in 2019. His research is focused on advanced, low-cost electrodes for both lithium-ion batteries and sodium-ion batteries.



Shu-Lei Chou is currently an associate professor at the Institute for Superconducting and Electronic Materials, University of Wollongong. He received his Ph.D. degree from the University of Wollongong in 2010. His research interests include energy storage materials for battery applications, especially novel composite materials, new binders, and new electrolytes for Li/Na batteries.

2. Why is X-Ray Absorption Spectroscopy so Important for Battery Electrodes?

X-ray absorption spectroscopy is a widely used technique that measures the X-ray absorption coefficient of a specimen as a function of the X-ray photon energy, just above or below the exact absorption edge of a certain element. XAS is an inner shell spectroscopy, which means that an X-ray interacts primarily with a deep-core electron rather than with a valence electron. According to the energy level of the probing X-ray sources, XAS can be divided into three kinds of types: soft (< 1 keV), tender (1–5 keV), and hard XAS (> 5 keV). Also, an X-ray absorption spectrum can be classified into two regions: X-ray absorption near-edge structure (XANES) and extended X-ray absorption fine structure (EXAFS). XANES covers the range from the absorption edge to 50 eV above the edge, while EXAFS extends the range from 50 eV above the edge to as high as 1000 eV.^[15] The synchrotron-based XANES data offer high-resolution signals, which can provide valuable quantitative and/or qualitative information regarding the oxidation states of the cathode materials, as well as their site symmetries and coordination circumstances. EXAFS data can be employed to study the localised short-range structures, bond lengths, and distinctive chemical fingerprints of the nearest neighbours (normally several shell atoms) of the atoms absorbing the X-rays. Generally speaking, soft XAS is commonly used for low-Z elements such as C, N, O, etc., and hard XAS is more powerful when probing the K-edge or L-edge of 3d and 4d transition metals. Another great advantage of XAS over other advanced characterization methods is its elemental selectivity.^[16] It offers a feasible approach to detect the environment surroundings of the atoms of certain elements in XANES, even if neighbouring atoms in the periodic table are present (in the EXAFS signal they will be indistinguishable if the elements have similar electronic configuration). Therefore, due to its high elemental selectivity and high chemical sensitivity, XAS is an indispensable tool to fully understand the charge compensation/transition process in a cathode material containing multiple



Shi-Xue Dou is a distinguished professor and director at the Institute for Superconducting and Electronic Materials (ISEM) at the Australian Institute of Innovative Materials, University of Wollongong. He is program leader for Automotive CRC2020 and ARENA Smart Sodium Storage System program. His research focuses on energy and electronic materials.

elements that may be troublesome in other techniques. Furthermore, *in-situ* XAS can offer extra information on the main contributing element of a redox process in continuous charge/discharge. Speaking overall, XAS data can provide detailed chemical and physical information over a short range, which is critical for selecting appropriate orientations to improve the electrochemical performance of various cathode materials as well as discovering and designing novel electrodes for SIBs towards their real applications in the near future.

3. XAS Techniques for Sodium Layered Transition Metal Oxides

Na_xTMO_2 layered oxides ($0 < x \leq 1$; TM=Cr, Co, Fe, V, Mg, Zn, Mn, Ni, V, etc. and mixtures of them)) are one of the most important branches of the cathode family of SIBs. They possess high theoretical capacities, appropriate working voltage platforms, and highly scalable synthesis approaches. Most of the 3d transition elements are electrochemically active in various layered structures (normally P2 types or O3 types according to the coordination circumstances).^[9] Nevertheless, the Na_xTMO_2 layered oxides are still facing three major challenges for their further development: (1) irreversible phase transitions; (2) storage instability; and (3) insufficient/degraded battery performance. These main obstacles cannot be well addressed without achieving a fundamental and comprehensive understanding of their causes, focused on changes in the short-range local structure. Therefore, in order to solve these problems, synchrotron-based XAS should be primarily employed to obtain the precise valence changes as well as information on the corresponding atomic coordination.

Komaba et al. employed the XAS technique to detect the charge compensation mechanisms during cycling. They found a clear shift towards the higher energy region of the Mn K-edge after charging to 3.8 V, which means that in the P2- $\text{Na}_x[\text{Fe}_{1/2}\text{Mn}_{1/2}]\text{O}_2$ system, the charge compensation is mainly achieved by oxidation of Mn. They also observed the same tendency for Fe, indicating that the $\text{Fe}^{3+}/\text{Fe}^{4+}$ redox couple exists in the sodium layered oxides (Figure 2a–b).^[17] From the XAFS spectra, the bond length of Fe–O only changes when the oxidation state is over 4.2 V. This will incur a non-cooperative Jahn-Teller effect on the oxidized high-spin Fe^{4+} ($t_{2g}^3 e_g^1$), which cannot be realized in O3- LiFeO_2 , since the Fe^{3+} 3d-orbital is firmly hybridized with the O 2p orbital (Figure 2c). Similarly, Delmas's group determined the structural evolution and redox mechanisms of O3- $\text{Na}_x\text{Mn}_{1/3}\text{Fe}_{2/3}\text{O}_2$ upon Na^+ de/intercalation. Through operando XANES, they found that there is an obvious two stage process that can be observed in Fe K-edge spectra. For $0.670 < x \leq 1$, only the $\text{Mn}^{3+}/\text{Mn}^{4+}$ redox reaction appears; while for $x < 0.670$, the $\text{Fe}^{3+}/\text{Fe}^{4+}$ reaction only occurs after full oxidation of Mn^{3+} ions (Figure 2d–f).^[18] This deduction still needs further assessments by other characterization methods, however. Hu's group systematically investigated Fe-based tunnel-type $\text{Na}_{0.61}[\text{Mn}_{0.27}\text{Fe}_{0.34}\text{Ti}_{0.39}]\text{O}_2$ and found that the shift is even more pronounced than that in P2-type $\text{Na}_{0.67}[\text{Fe}_{0.5}\text{Mn}_{0.5}]\text{O}_2$

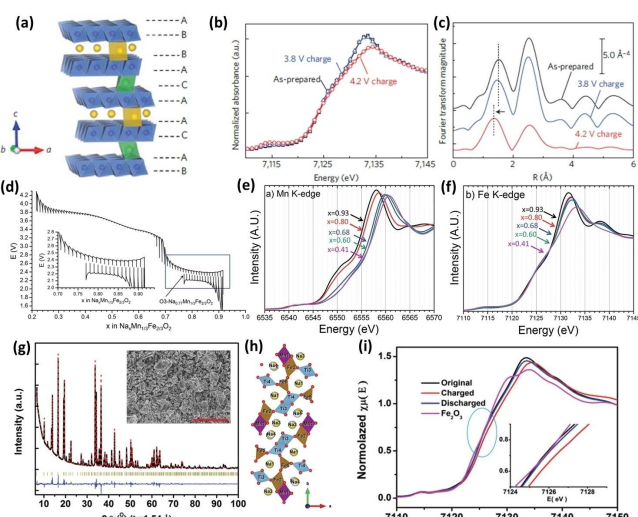


Figure 2. (a) Schematic illustration of P2-type $\text{Na}_{2/3}[\text{Fe}_{1/2}\text{Mn}_{1/2}]\text{O}_2$. (b) XANES and (c) EXAFS spectra of the P2-type $\text{Na}_x[\text{Fe}_{1/2}\text{Mn}_{1/2}]\text{O}_2$ samples at cut-off voltages of 3.8 V and 4.2 V, respectively. Reprinted with permission from (a)–(c).^[17] Copyright 2012 Springer Nature. (d) Galvanostatic intermittent titration technique (GITT) cycling curve of the O3-type $\text{Na}_x\text{Mn}_{1/3}\text{Fe}_{2/3}\text{O}_2$ system. (e) and (f) Operando *in-situ* XANES and EXAFS spectra of the Fe K-edge of a $\text{Na}/\text{Na}_x\text{Mn}_{1/3}\text{Fe}_{2/3}\text{O}_2$ battery, respectively. Reprinted with permission from (d)–(f).^[18] Copyright 2015 Royal Society of Chemistry. (g) X-ray diffraction (XRD) pattern and Rietveld refinement of tunnel-type $\text{Na}_{0.61}[\text{Mn}_{0.27}\text{Fe}_{0.34}\text{Ti}_{0.39}]\text{O}_2$ sample and (h) corresponding schematic illustration along the [001] direction. (i) XANES spectra of Fe–K edge with different states of charge. Reprinted with permission from (g)–(i).^[19] Copyright 2015 WILEY-VCH.

layered oxides (Figure 2g–i). A highly reversible $\text{Fe}^{3+}/\text{Fe}^{4+}$ redox couple in tunnel type oxides was confirmed via EXAFS analysis. They also conducted *ex-situ* XANES of Mn and Ti at the same time and found that Mn participated in charge compensation while Ti remained unchanged.^[19]

Recently Kang's group discovered a new iron-based intercalation host for advanced LIBs. They showed that cubic-FeOF electrode is highly electrochemical active. It is believed that this cubic-FeOF electrode is also reversible in SIBs.^[20]

Zhao et al. investigated the influence of the synthesis conditions of P2-type Fe-based $\text{Na}_{2/3}\text{Fe}_{2/3}\text{Mn}_{1/3}\text{O}_2$ for SIBs. They found that for quenched and one-step calcined samples, a voltage plateau of 2.5 V appeared, which was mainly attributed to the $\text{Mn}^{3+}/\text{Mn}^{4+}$ redox couple. From the XANES spectra, no obvious influence of Fe could be detected, while derivative curves of Mn K-edge spectra was observed as well as the corresponding charge/discharge curves (Figure 3a–c).^[21] The $\text{Fe}^{3+}/\text{Fe}^{4+}$ reversible redox couple is involved in the 3 V–4 V region, and the $\text{Mn}^{3+}/\text{Mn}^{4+}$ redox couple is mainly involved in the 2 V–3 V region. Mn plays important roles in all kinds of layered oxides, since the $\text{Mn}^{2+}/\text{Mn}^{3+}/\text{Mn}^{4+}$ redox couples can offer satisfactory theoretical capacities over a wide range of voltage windows. Song et al. systematically investigated a novel P3-type $\text{Na}_{2/3}\text{Mg}_{1/3}\text{Mn}_{2/3}\text{O}_2$ cathode with reversible oxygen redox reactions.^[22] This material possesses a discharge capacity of over 220 mAh g⁻¹ when the $\text{Mn}^{3+}/\text{Mn}^{4+}$ redox is involved in the oxygen redox reaction. The oxygen redox reaction can be more easily achieved via the participation of Mg^{2+} , which has

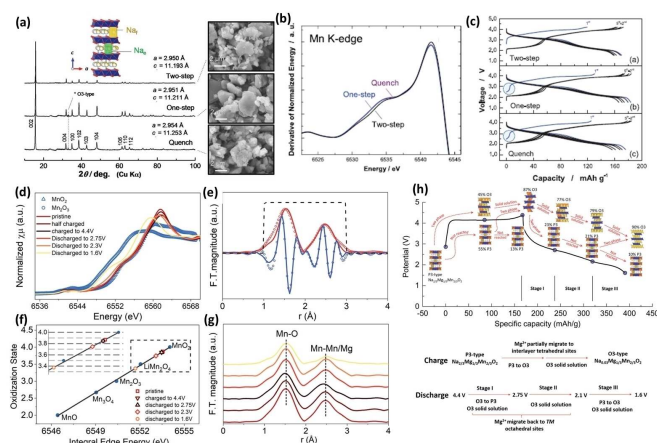


Figure 3. (a) XRD patterns of P2-type $\text{Na}_{2/3}[\text{Fe}_{2/3}\text{Mn}_{1/3}] \text{O}_2$ samples synthesized under different conditions with corresponding scanning electron microscope (SEM) images. (b) Derivative Mn K-edge XAS spectra and (c) galvanostatic charge/discharge curves of P3-type $\text{Na}_{2/3}[\text{Fe}_{2/3}\text{Mn}_{1/3}] \text{O}_2$ samples synthesized under different conditions at room temperature. Reprinted with permission from (a)–(c).^[21] Copyright 2018 WILEY-VCH. (d) XANES spectra of P3-type $\text{Na}_{2/3}\text{Mg}_{1/3}\text{Mn}_{2/3}\text{O}_2$ at different states of charge. (e) Fourier transform (FT)-EXAFS using the structure derived from XRD. (f) Fitted curves of Mn valence at various states of charge. (g) Mn–O bonding and Mn–Mn/Mg bonding information from EXAFS. (h) Schematic illustration of phase transformation within the initial cycle. Reprinted with permission from (d)–(h).^[22] Copyright 2019 Royal Society of Chemistry.

stronger ionic bonding with oxygen. They proposed that, during the initial cycle, the capacity is mainly attributable to the reversible oxygen redox reaction rather than the $\text{Mn}^{3+}/\text{Mn}^{4+}$ redox couple, which was further confirmed via XANES spectra. Mn is the Mn^{4+} state initially, and there is an obvious discrepancy even after charging to 4.4 V (Figure 3d). With the help of FT-EXAFS, Mg and Mn were confirmed to be ordered distributed, while the Mn–O bond length decreased gradually (Figure 3e–g).

In addition, they proposed a phase transition mechanism of this P3-type $\text{Na}_{2/3}[\text{Fe}_{2/3}\text{Mn}_{1/3}] \text{O}_2$ material. The ion migration is obvious within the first cycle (with Mg^{2+} partially migrating to interlayer tetrahedral sites, Figure 3h). Hu's group recently reported a strategy for suppressing the voltage decay of P2-type $\text{Na}_{0.7}[\text{Cu}_{0.15}\text{Fe}_{0.3}\text{Mn}_{0.55}] \text{O}_2$.^[23] Fe³⁺ migration to neighbouring tetrahedral sites will incur inevitable voltage decay. A higher cut-off voltage will trigger a drastic phase transition. They employed the advanced X-ray pair distribution function (PDF) and hard/soft XAS to further determine how the doped Cu could bring more capacity via correlation with ligand transition metals and ligand oxygen. Mn^{4+} was found to be essentially unchanged, with only a tiny amount of Mn^{4+} reduced. Fe ions tend to remain in the interlayer tetrahedral sites, however, leading to larger polarization and a severe voltage fading phenomenon. The soft XAS spectra indicated that the increased Cu content could enhance the metal to ligand charge transfer (MLCT) effect, and the O K-edge also showed that Cu–O becomes a redox centre compensating for charge neutrality (as a result of Fe ion migration). It can be deduced that other transition metal elements such as Zn, Ti, and Ru will also have

positive effects on the voltage decay mentioned above.^[24–26] Multiple element doping can also reduce the Jahn-Teller effect.

Mn is troublesome sometimes since the strong Jahn-Teller effect from manganese (III) centres can destabilize host structures. Very recently, Kang's group reported that Li/Zn substitution can be an effective way to reduce the inherent phase separation.^[26] A high binding energy was confirmed, and octahedral structure variations were reduced. An oxidation state with low average energy was examined via *ex-situ* XANES. In the EXAFS spectra, an additional peak around 0.98 Å was observed for the pristine sample, while there was no additional peak for the Zn-doped sample, indicating that the Jahn-Teller distortion was suppressed to a certain degree (Figure 4a–c). Multiple element doping can also reduce the Jahn-Teller effect.^[27–29] Ma's

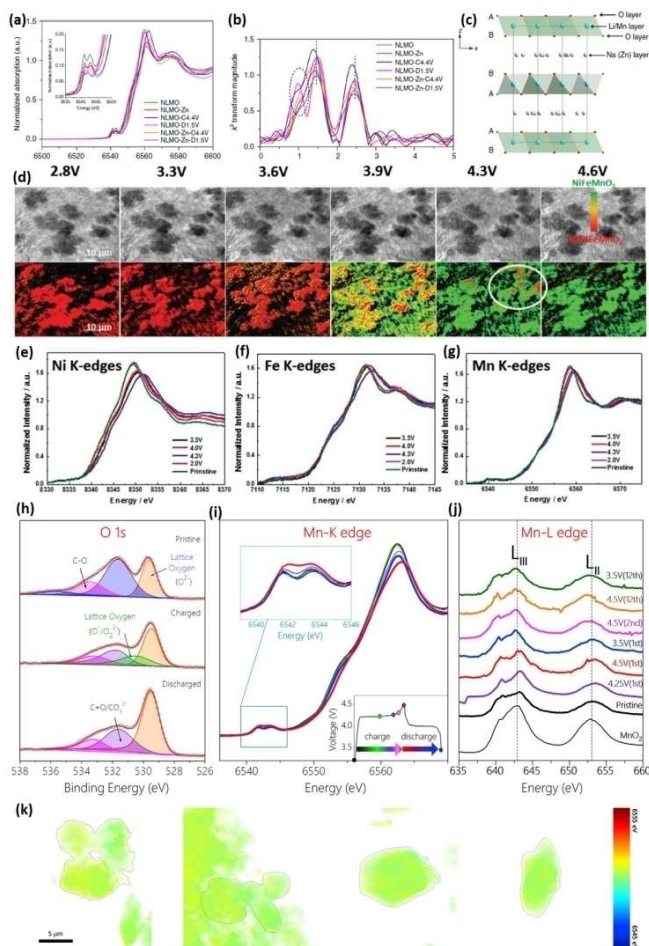


Figure 4. (a) XANES and (b) EXAFS spectra at the Mn K-edge of Zn-doped NLMO sample. (c) Crystal structure of Zn-doped P2-type NLMO along the [001] orientation. Reprinted with permission from (a)–(c).^[26] Copyright 2019 Springer Nature. (d) Morphology evolution and chemical phase mapping via operando TXM technique of $\text{Na}_{1-x}\text{Ni}_{1/3}\text{Fe}_{1/3}\text{Mn}_{1/3}\text{O}_2$ material. (e) Ni K-edge, (f) Fe K-edge, (g) Mn K-edge *ex-situ* XANES spectra of pristine and cycled $\text{Na}_{1-x}\text{Ni}_{1/3}\text{Fe}_{1/3}\text{Mn}_{1/3}\text{O}_2$ material. Reprinted with permission from (d)–(g).^[30] Copyright 2016 WILEY-VCH. (h) XPS O 1s spectra of P3-type $\text{Na}_{1-x}\text{Ni}_{1/3}\text{Fe}_{1/3}\text{Mn}_{1/3}\text{O}_2$ material in different states of charge. (b) Mn K-edge and (c) Mn L-edge during cycling. (k) two-dimensional (2D) nanoscale XAS mapping of Mn oxidation states after different numbers of cycles. Reprinted with permission from (h)–(k).^[34] Copyright 2017 Elsevier Inc.

group employed operando transmission X-ray microscopy (TXM) techniques and *ex-situ* XANES spectra to investigate a proposed nonequilibrium solid solution of $\text{Na}_{1-\delta}\text{Ni}_{1/3}\text{Fe}_{1/3}\text{Mn}_{1/3}\text{O}_2$.^[30] Full-field TXM-XANES images of the Fe K-edge (7131 eV) and Ni K-edge (8333 eV) at different sweep speeds were collected. The sodium was continuously removed during the charging process, and two separate thermodynamic phases were identified with distinct red and green colours (Figure 4d). Also, from the *ex-situ* XANES spectra, the $\text{Fe}^{3+}/\text{Fe}^{4+}$ reaction only occurs after full oxidation of Ni^{2+} , and there are no significant variations for the Mn K-edge (Figure 4e-g). Similar findings were revealed recently.^[31-33] Rong et al. reported a P3-type $\text{Na}_{0.6}[\text{Li}_{0.2}\text{Mn}_{0.8}]\text{O}_2$ material with relatively weak Mn–O covalent bonding. Participation of an anionic redox reaction (ARR) was determined and analysed in detail, using the neutron pair distribution function (PDF) and hard/soft XAS.^[34] Obvious oxygen bonding environments were observed in the O 1s X-ray XPS spectrum (Figure 4h), and the valence of Mn remained unchanged after cycling. From the transition metal L-edge (electric dipole-allowed 2p–3d transition), it could be deduced that weakened Mn–O hybridization may be the main reason for the oxygen redox reaction (Figure 4i–j). They also investigated the exact Mn oxidation state via the two-dimensional nanoscale XANES mapping technique. The average values of the edge energy of Mn were all close to MnO_2 , indicating that Mn ions tend to remain in the Mn^{4+} state, while the ARR may take place in the reaction instead (Figure 4k). This work highlighted the achievable approach of suppressing and restricting the electrochemical activity of Mn^{4+} in Mn-based P3-type layered oxides. Other work also highlighted the importance of the oxygen redox chemistry.^[35-38]

Cr-based layered oxides can exhibit high reversible specific capacities. Ding et al. improved their cycling performance by carbon coating and charge compensation through Cr–Cr and Cr–O bonds.^[39] Zhou et al. explored their structural evolution through *ex-situ* XAS spectra and found that the $\text{Cr}^{3+}/\text{Cr}^{3.5+}$ redox couple is electrochemically active and that Cr ions tend to stay on octahedral sites.^[40] Cao et al. reported the $\text{Cr}^{2.8+}/\text{Cr}^{4+}$ redox couple in O3-type $\text{Na}_{0.66}\text{Fe}_{1/3}\text{Cr}_{1/3}\text{Ti}_{1/3}\text{O}_2$ material for SIBs.^[41] With the help of XAS spectra, they found that redox processes only occurred with $\text{Cr}^{2.8+}/\text{Cr}^{4+}$ while Ti^{4+} and Fe^{3+} remained as stabilizers without change. The Cr–O bond lengths cannot be fully restored, while the bond lengths of Fe–O and Ti–O are almost invariable. Then, researchers also paid many attentions to the $\text{Co}^{2+}/\text{Co}^{3+}$ redox couple. Cheng et al. explored a P2- $\text{Na}_{2/3}\text{Co}_{2/3}\text{Mn}_{1/3}\text{O}_2$ material and found that the valences of Co and Mn were initially +III and +IV, respectively, and that both $\text{Co}^{3+}/\text{Co}^{2+}$ and $\text{Mn}^{4+}/\text{Mn}^{3+}$ are involved in the electrochemical reactions.^[42] In Na_xCoO_2 materials, Co–O bonds become softer during cycling, while the Co–Co bonds hardly show any obvious discrepancy.^[43,44] Wang et al. investigated the $\text{Co}^{2+}/\text{Co}^{3+}$ redox couple in P2-type $\text{Na}_{0.66}\text{Co}_{0.22}\text{Mn}_{0.44}\text{Ti}_{0.34}\text{O}_2$. With the increasing Co contents from $x=0$ to 0.33 in $\text{Na}_{0.66}\text{Co}_x\text{Mn}_{0.66-x}\text{Ti}_{0.34}\text{O}_2$, the crystal structure tends to transform from orthorhombic to hexagonal.^[45] From the XANES spectra, the low valence of Co^{2+} substitution can favour Mn in the high valence state of +4, which will reduce the distortion of the Jahn-Teller effect of Mn^{3+} . Charge compensation indicates that the capacity should mainly attributed to $\text{Co}^{2.2+}/\text{Co}^{3+}$ and $\text{Mn}^{3.3+}$ /

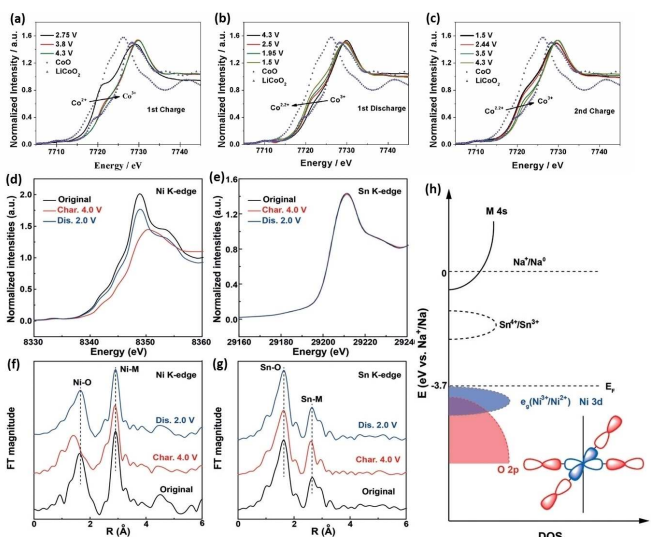


Figure 5. (a), (b), and (c) Co K-edge XANES of NCMT-2 material at different stages of charge/discharge. Reprinted with permission from (a)–(c).^[45] Copyright 2017 Authors & WILEY-VCH. (d) XANES spectra of Ni K-edge and (e) Sn K-edge of $\text{Na}_{0.7}\text{Ni}_{0.35}\text{Sn}_{0.65}\text{O}_2$. (f) and (g) Corresponding EXAFS spectra. (h) Molecular orbitals and electronic structure of $\text{Na}_{0.7}\text{Ni}_{0.35}\text{Sn}_{0.65}\text{O}_2$. Reprinted with permission from (d)–(h).^[46] Copyright 2018 WILEY-VCH.

$/\text{Mn}^{4+}$ (Figure 5a–c). Developing a high voltage O3-type with high initial cycle Coulombic efficiency is of great importance for high energy density SIBs. Guo's group recently reported a new family of O3-type cathodes with the general formula $\text{Na}_x\text{Ni}_{x/2}\text{Sn}_{1-x/2}\text{O}_2$.^[46] The $\text{Ni}^{2+}/\text{Ni}^{3+}$ potential was abnormally located at 3.7 V (vs. Na^+/Na), which is proposed to result from the reduced hybridization between O 2p and M 3d orbitals in stacked MO_2 layers. $\text{Ni}^{2+}/\text{Ni}^{3+}$ is responsible for the detected charge compensation in the voltage window of 2.0–4.0 V, while Sn K-edge XANES spectra did not show any obvious changes (Figure 5d–g). Sn^{4+} is filled with 3d¹⁰ electrons and did not take part in hybridization with MO_2 stacking layers, while only Ni e_g orbitals hybridize O 2p orbitals, so that higher electronic density on O can be created through enhanced Ni–O bond ionicity (Figure 5h).

XAS is heavily involved in the investigations of layered oxide materials for advanced SIBs. This technique is essential and irreplaceable due to its high selectivity and high sensitivity, which is important for determining specific and subtle structural information over a very short range. We hope to see more relevant work reported with the aim of addressing the obstacles and challenges mentioned above.

4. XAS Techniques for Polyanionic-Based Cathode Materials for SIBs

Compounds with a polyanionic-based framework are one of the most important branches of advanced cathode materials for SIBs.^[3,10,47] They possess a robust framework with sturdy corner- or edge-sharing MO_6 ($M=3\text{d}$ transition metal) octahedra and XO_4 ($\text{X}=\text{Si}, \text{S}, \text{P}, \text{Se}$, etc.) tetrahedra.^[3,48] Their three-

dimensional (3D) framework not only can provide small volume change, but also is thermally safe under extreme circumstances due to their non-flammable nature. The XAS technique is extensively used in this type of material because of the oxidation states of transition metals as well as their corresponding coordination situations.^[49]

Vanadium-based polyanionic materials have become very important in recent years. In 2013, Rojo's group initially studied the electrochemical Na storage mechanism of $\text{Na}_3\text{V}_2\text{O}_{2x}(\text{PO}_4)_2\text{F}_{3-x}$. They found that the vanadium oxidation state of V in the pristine sample was around +3.8 and that the $\text{V}^{4+}/\text{V}^5+$ redox couple was responsible for the charge compensation. A forbidden transition from 1s to 3d was found in the pre-edge region, which means that the V^{3+} ions (~18% of the total V ions) in the pristine sample remained unchanged, while V^{4+} (~82% to total V ions) was progressively oxidized and converted to V^{5+} .^[50] Then Broux et al. presented a detailed study on $\text{Na}_3\text{V}_2(\text{PO}_4)_2\text{F}_3$ by operando XAS, since it has the highest theoretical energy density.^[51] An overall shift of 2.5 eV on the main absorption edge was observed due to increased 3d–4p orbital mixing with progressive distortion of the local symmetry (Figure 6a–b). Whittingham's group investigated Mo-doped ϵ -VOPO₄ material. They found that the major discrepancy appeared in the pre-edge area since more symmetric VO₆ octahedra remained in the low-voltage region (Figure 6c–e).^[52] Cao's group successfully synthesized a fully sodiated NaVOPO₄ material with layered structure for SIBs. The reversible pre-edge peak indicated that the $\text{V}^{4+}/\text{V}^5+$ redox couple is the main electrochemical centre (Figure 6f).^[53] Taras-

con's group electrochemically synthesized the disordered $\text{Na}_3\text{V}_2(\text{PO}_4)_2\text{F}_3$ material with tetragonal symmetry (I4/mmm space group).

In the voltage window of 1 to 4.8 V, this new synthesized phase can enable 3 sodium ions to transfer per formula unit. Disordered phase was determined from the initial charge state, while the vanadium state varied from +3 to +4.5.^[54] The refined structures are shown in Figure 6g. Wang et al. recently demonstrated a symmetric cell with sodium superionic conductor (NASICON)-structured $\text{Na}_2\text{Ti}(\text{PO}_4)_3$ via a facile sol-gel method.^[55] They employed in-situ synchrotron XRD to determine the phase change and found that three main phase regions appeared (Figure 6h). Also, from the in-situ XANES spectra (Figure 6i), the valence of Ti remained unchanged above 3.1 V, and $\text{V}^{3+}/\text{V}^{4+}$ was the dominant redox couple accounting for the charge compensation. The $\text{Ti}^{3+}/\text{Ti}^{4+}$ redox couple was confirmed in the voltage window of 2.0–3.1 V. Other researchers also did splendid work on the characterization of vanadium states in various structures or frameworks.^[56–59] It can be reasonably expected that more relevant work regarding the state changes of vanadium will be reported with higher voltage potentials and higher energy densities for SIBs.

Another important element in the polyanionic-based materials is iron, since the $\text{Fe}^{2+}/\text{Fe}^{3+}$ redox couple is highly electrochemically active in most structures and chemical environments. In 2013, Kang's group reported the mixed polyanion framework material $\text{Na}_4\text{Fe}_3(\text{PO}_4)_2(\text{P}_2\text{O}_7)$ with a one-phase reaction through the $\text{Fe}^{2+}/\text{Fe}^{3+}$ redox couple. It possessed a robust structure even when heated up to 530 °C, and the XANES spectra further confirmed that the $\text{Fe}^{2+}/\text{Fe}^{3+}$ redox couple is reasonable for the charge compensation.^[60] Yamada's group systematically investigated an alluaudite-type sodium iron sulfate material, $\text{Na}_2\text{Fe}_2(\text{SO}_4)_3$. This material possesses a high voltage platform around 3.8 V with 2D Na⁺ ion diffusion pathways. From the XANES spectra, Fe was shifted toward higher energy during charging, and no isosbestic points were observed, indicating a single phase transition process.^[61] Other types of Fe-based polyanionic materials were also investigated recently.^[59,62–64]

XAS is a powerful tool to determine the valence changes and corresponding orbital hybridization situations, which is helpful to obtain detailed information on specific elements in the polyanionic type cathode materials. For example, appropriate doping elements can sustain or be fixed at a certain valence, which would be essential for stabilization of the crystal structure under various electrochemical conditions. Also the pre-edge area can provide extra information on orbital hybridization, and this can be considered as solid evidence of iron migration in certain types of materials within the initial cycle. However, it should be noted that the high sensitivity of the edge position to the oxidation state holds only for TM with comparatively low absorption edge energy < 10 keV. Higher edge energy lead to much shortened lifetime which results in a much lower energy resolution. This strongly limits the amount of information that can be deduced from the XANES. More

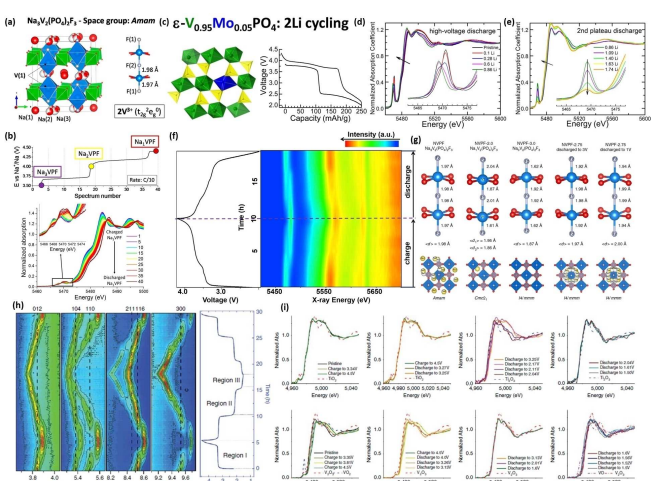


Figure 6. (a) Crystal structure of $\text{Na}_3\text{V}_2(\text{PO}_4)_2\text{F}_3$ with space group Amm. (b) K-edge XANES spectra at C/10. Reprinted with permission from (a) to (b).^[51] Copyright 2017 American Chemical Society. (c) Crystal structure of ϵ -VOPO₄ and corresponding charge/discharge curve. V K-edge in-situ XAS spectra of Mo_{0.05}V_{0.95}OPO₄ for (d) high-voltage discharge and (e) low-voltage discharge. Reprinted with permission from (c) to (e).^[52] Copyright 2016 American Chemical Society. (f) Normalized XANES spectra (2D contour plot) collected during cycling. Reprinted with permission from (f).^[53] Copyright 2018 Elsevier Inc. (g) V–F bond lengths of pristine material, NVPF-2.0, NVPF-3.0, NVPF-2.75 discharged to 3.0 V, and NVPF-2.75 discharged to 1.0 V. Reprinted with permission from (g).^[54] Copyright 2019 Springer Nature. (h) Contour maps of in-situ synchrotron XRD during the initial cycle for a $\text{Na}/\text{Na}_2\text{VTi}(\text{PO}_4)_3$ half cell. (i) In-situ XANES spectra of Ti K-edge and V K-edge. Reprinted with permission from (h) to (i).^[55] Copyright 2017 Springer Nature.

relevant work can reasonably be expected with more information and guidance that the XAS technique can provide.

5. XAS Techniques for Prussian Blue Analogues for SIBs

Prussian blue analogues (PBAs) are important and promising cathode candidates for SIBs because of their long cycle life and rapid kinetics. The general chemical formula can be regarded as $A_xP_y[R(CN)_6]_z \cdot nH_2O$, where A is Na or K, while P and R are transition metals. They possess cubic structures with an open framework composed of octahedral hexacyanometalate complex bonded with C–N pairs. The intrinsic nature of their 3D Na^+ ion diffusion pathways gives them highly reversible rate performance. The XAS technique is an ideal tool that can be tuned for specific elements, and their distinctive contributions to their overall electrochemical activity can be quantified.

Goodenough's group investigated air-stable rhombohedral Prussian white as a cathode candidate for SIBs. They improved the sodium content in the formula, and they synthesized $R\text{-Na}_{1.92}\text{Fe}[\text{Fe}(\text{CN})_6]$ as the target material (Figure 7a).^[65] Two distinctive working potentials appeared, indicating that high spin FeN_6 octahedra and low spin FeC_6 octahedra are responsible for the two phase reaction (Figure 7b). Synchrotron-based soft XAS showed Fe L-edge spectra within two cycles. It was confirmed that the low-voltage platform corre-

sponds to FeN_6 octahedra, while FeC_6 is responsible for the high-voltage plateau (Figure 7c). C K-edge and N K-edge soft XAS spectra revealed that the electron states in the samples are highly itinerant (Figure 7d). Guo's group also focused on sodium iron hexacyanoferrate with high Na content. Fe K-edge EXAFS spectra indicated that sufficient Na^+ ions occupy the interstitial sites in the lattice.^[66] Mullaliu et al. recently studied the copper electroactivity through operando XAS.^[67] The crystal structure of the as-synthesized copper hexacyanoferrate is shown in Figure 7e. During cycling, cations in 8c position (both potassium and copper ions) are removed from the hexacyanoferrate structure. The Fe K-edge and copper K-edge spectra showed reversible variations in both the pre-edge region and the main absorption region (Figure 7f–h). The EXAFS data gave evidence of structural stability and low lattice strain.

Manganese-based PBA cathode is another important branch due to its high rate capability and higher voltage platforms. Firouzi et al. synthesized $\text{Na}_{1.24}\text{Mn}[\text{Mn}(\text{CN})_{6}]_{0.81} \cdot 2.1\text{H}_2\text{O}$ with 13 wt.% water content (Figure 7i).^[68] They employed soft XAS to probe the $\text{Mn}^{1+}/\text{Mn}^{2+}$ couple as well as the hybridization situation in the as-prepared MnHCMn electrodes. Figure 7j shows the Mn L_3 -edge (left) and the N K-edge (right) from soft XAS spectra, and both the high spin Mn^{II} system and the carbon-coordinated low spin $\text{Mn}(\text{C})$ system exist in this material. $\text{Mn}^{II}(\text{C})$ sits at a slightly lower energy, while $\text{Mn}^{II}(\text{N})$ is not electrochemically active during cycling. The novel $\text{Mn}^{1+}/\text{Mn}^{2+}$ redox couple can be considered as a promising redox centre for both anode and cathode materials. Another strategy for improving the electrochemical performance is to optimally expose specific crystal planes and confine the particles in a highly conductive matrix. Wang et al. synthesized the $\text{K}_{0.33}\text{FeFe}(\text{CN})_6$, which had (100) planes exposed and was wrapped in reduced graphene oxide.^[69] It possessed a highly reversible specific capacity of 160 mAhg^{-1} at 0.5 C. From the EXAFS spectra, Fe–C, Fe–N, Fe–K, and Fe–Fe shells could be recognized (Figure 7k).

Other researchers also have done tremendous work on the PBA cathodes with the help of advanced XAS techniques. Wu et al. introduced a method for modifying transition-metal redox reactions via interstitial water.^[70] They employed soft XAS and theoretical calculations to determine the influence of crystallized water in the structure. Distinct transition-metal redox sequences in hydrated material were found with different working platforms, while only one mixed potential appeared in anhydrous material. From both Fe L_3 -edge and Mn L_3 -edge soft XAS, it could be observed and analysed that the $\text{Fe}^{2+}/\text{Fe}^{3+}$ reaction had been completed at a low voltage plateau for hydrated material, but only about 50% of the Fe ions were oxidized in the unhydrated material. The $\text{Mn}^{2+}/\text{Mn}^{3+}$ redox couple reactions took place at a high state of charge in the hydrated system; the oxidation of both Mn and Fe gradually increased during the whole charging process. Similar works were reported by other researchers recently.^[71–76]

The spin state and coordination circumstances are critical for the final electrochemical performance of PBAs. Therefore, achieving an in-depth understanding is essential to provide better guidance for optimizing their formula, water content,

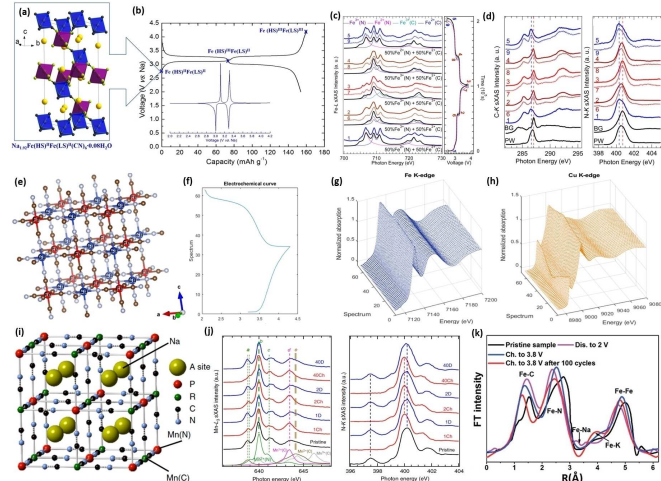


Figure 7. (a) Crystal structure of $R\text{-Na}_{1.92}\text{Fe}[\text{Fe}(\text{CN})_6]$ material and (b) corresponding electrochemical profile. (c) Fe L-edge soft XAS (sxAS) and (d) N K-edge sXAS spectra of various electrochemical states. Reprinted with permission from (a)–(d).^[65] Copyright 2015 American Chemical Society. (e) Repeated atomic fragments of $\text{Cu}[\text{Fe}(\text{CN})_6](\text{NO}_3)$ material and (f) corresponding electrochemical profile. (g) Fe K-edge and Cu K-edge XAS spectra during cycling. Reprinted with permission from (e)–(h).^[67] Copyright 2018 American Chemical Society. (i) Crystal structure of $\text{Na}_{1.24}\text{Mn}[\text{Mn}(\text{CN})_6]_{0.81} \cdot 2.1\text{H}_2\text{O}$. (j) Mn L_3 -edge sxAS spectra (left) and N K-edge sxAS spectra (right) at different states of charge. Reprinted with permission from (i)–(j).^[68] Copyright 2018 Springer Nature. (k) EXAFS K-edge spectra of the as-prepared $\text{K}_{0.33}\text{FeFe}(\text{CN})_6$ reduced graphene oxide (rGO) material at various states of charges. Reprinted with permission from (k).^[69] Copyright 2017 Royal Society of Chemistry.

etc. The XAS technique is an irreplaceable tool to find out the truth, as we have mentioned. We can reasonably anticipate that more comprehensive or sophisticated work on PBAs will be published in the near future regarding better electrochemical performances.

6. Summary and Perspectives

SIBs have witnessed tremendous progress on cathodes, anodes, and electrolytes in recent years. There is still a long way to go, however, before industrial level manufacturing of SIBs becomes a reality. In order to meet the requirements of applications, such as satisfactory cycling stability, high energy density, and good rate performance, the selection and optimization of cathode materials are the most challenging aspects of full cell performance. Appropriate and effective modifications and/or discoveries cannot be achieved to any great extent without a comprehensive and deep understanding of their various complicated structures and atoms coordination. Therefore, advanced characterization techniques are necessary tools for the further understandings and investigation of SIBs. Synchrotron-based techniques are playing more and more important roles in characterizing cathode materials due to their high-resolution signals and short data collection time. Among them, both hard and soft XAS are more and more widely used because of their elemental selectivity and high chemical sensitivity. In addition, in-situ or operando XAS can provide real-time information on the chemical environment and oxidation state of a target element, even multiple elements that are present simultaneously at certain charge/discharge rates.

Three main types of cathode materials, namely layered oxides, polyanions, and Prussian blue analogues, have been summarized and discussed in detail in relation to advanced XAS techniques. From the XANES spectra, the valence state of a specific element involved in redox reactions can be clearly observed and verified. For layered oxides, it is important to determine the exact oxidation states of transition metal elements, so that insightful guidance can be obtained to better improve their overall electrochemical performance. In the case of polyanions and Prussian blue analogues, the spin state as well as the coordination information is critical for tuneable voltage profiles and improved electrochemical activity.^[77,78] From EXAFS spectra, local structural changes can be monitored, such as specific bond lengths, and octahedral or tetrahedral distortions of all three types of cathode materials. Soft XAS is also inherently sensitive to the occupied and unoccupied electron orbitals above the Fermi level, especially electric dipole-allowed 2p-3d transition hybridizations (L-edge). The light elements such as Na, C, O, and N can be measured at the same time. Soft XAS is also flexible, with various probing depths (from surface to bulk, up to 0.1 μm) through different signal detection modes (the self-absorption problematic and the need to work under vacuum to reduce air absorption in soft XAS are still troublesome). Thus, valuable information on

multi-phase reactions and inhomogeneous reactions can be provided and analysed for all kinds of cathodes.

The combination of different synchrotron-based characterization methods will surely create a roadmap for new discoveries in the cathode research field for SIBs. Other advanced techniques, such as scanning transmission electron microscopy (STEM) and solid-state nuclear magnetic resonance (SS NMR), are also ideal supporting tools to further verify and consolidate the novel findings from the XAS spectra. There is still room, however, for further development of the XAS technique: (1) the designs of in-situ cells can be more simple and friendly; (2) in-situ soft XAS experiments still demand a high vacuum environment; (3) beam damage is still troublesome for some types of cathode materials, so that high-speed data collection is required; and (4) new strategies need to be developed to probe the non-equilibrium states of SIBs. All in all, by summarizing the development of and progress on SIBs through synchrotron-based X-ray absorption spectroscopy, we hope that this review will throw light upon on the exciting novel discoveries of electrodes for SIBs that have been reported.

Acknowledgements

This work is supported by the Australian Automotive Cooperative Research Centre and the Malaysian Automotive Institute (AutoCRC/MAI Project Agreement 1-111: Development of Advanced Electrode and Electrolytes for the LIB), the Australian Research Council (ARC DP160102627), and the Australian Renewable Energy Agency (ARENA S4 project). The authors would like to thank Dr. Tania Silver for critical reading of the manuscript.

Conflict of Interest

The authors declare no conflict of interest.

Keywords: X-Ray absorption spectroscopy · sodium storage mechanism · cathode · sodium-ion batteries

- [1] M. Armand, J.-M. Tarascon, *Nature* **2008**, *451*, 652–657.
- [2] Z. P. Cano, D. Banham, S. Ye, A. Hintennach, J. Lu, M. Fowler, Z. Chen, *Nat. Energy*, **2018**, *3*, 279–289.
- [3] J. Y. Hwang, S. T. Myung, Y. K. Sun, *Chem. Soc. Rev.* **2017**, *46*, 3529–3614.
- [4] Q. Liu, Z. Hu, M. Chen, C. Zou, H. Jin, S. Wang, S. L. Chou, S. X. Dou, *Small* **2019**, *15*, 1805381.
- [5] M. Chen, D. Cortie, Z. Hu, H. Jin, S. Wang, Q. Gu, W. Hua, E. Wang, W. Lai, L. Chen, S.-L. Chou, X.-L. Wang, S.-X. Dou, *Adv. Energy Mater.* **2018**, *8*, 1800944.
- [6] M. Chen, L. Chen, Z. Hu, Q. Liu, B. Zhang, Y. Hu, Q. Gu, J.-L. Wang, L.-Z. Wang, X. Guo, S.-L. Chou, S.-X. Dou, *Adv. Mater.* **2017**, *29*, 1605535.
- [7] Y. Yuan, K. Amine, J. Lu, R. Shahbazian-Yassar, *Nat. Commun.* **2017**, *8*, 15806.
- [8] S.-M. Bak, Z. Shadike, R. Lin, X. Yu, X.-Q. Yang, *NPG Asia Mater.* **2018**, *10*, 563–580.
- [9] M. Chen, Q. Liu, S.-W. Wang, E. Wang, X. Guo, S.-L. Chou, *Adv. Energy Mater.* **2019**, *9*, 1803609.

- [10] P. Barpanda, L. Lander, S.-i. Nishimura, A. Yamada, *Adv. Energy Mater.* **2018**, *8*, 1703055.
- [11] P. Wang, Y. You, Y. Yin, Y. Guo, *Adv. Energy Mater.* **2018**, *8*, 1701912.
- [12] B. Wang, Y. Han, X. Wang, N. Bahlawane, H. Pan, M. Yan, Y. Jiang, *iScience* **2018**, *3*, 110–133.
- [13] X. Liu, W. Yang, Z. Liu, *Adv. Mater.* **2014**, *26*, 7710–7729.
- [14] L. Yu, L. P. Wang, H. Liao, J. Wang, Z. Feng, O. Lev, J. S. C. Loo, M. T. Sougrati, Z. J. Xu, *Small* **2018**, *14*, 1703338.
- [15] Z. Shadike, E. Zhao, Y.-N. Zhou, X. Yu, Y. Yang, E. Hu, S. Bak, L. Gu, X.-Q. Yang, *Adv. Energy Mater.* **2018**, *8*, 1702588.
- [16] G.-L. Xu, R. Amine, A. Abouimrane, H. Che, M. Dahbi, Z.-F. Ma, I. Saadoune, J. Alami, W. L. Mattis, F. Pan, Z. Chen, K. Amine, *Adv. Energy Mater.* **2018**, *8*, 1702403.
- [17] N. Yabuuchi, M. Kajiyama, J. Iwatake, H. Nishikawa, S. Hitomi, R. Okuyama, R. Usui, Y. Yamada, S. Komaba, *Nat. Mater.* **2012**, *11*, 512–517.
- [18] B. Mortemard de Boisse, J. H. Cheng, D. Carlier, M. Guignard, C. J. Pan, S. Bordère, D. Filimonov, C. Drathen, E. Suard, B. J. Hwang, A. Wattiaux, C. Delmas, *J. Mater. Chem. A* **2015**, *3*, 10976–10989.
- [19] S. Xu, Y. Wang, L. Ben, Y. Lyu, N. Song, Z. Yang, Y. Li, L. Mu, H.-T. Yang, L. Gu, Y.-S. Hu, H. Li, Z.-H. Cheng, L. Chen, X. Huang, *Adv. Energy Mater.* **2015**, *5*, 1501156.
- [20] S.-K. Jung, I. Hwang, S.-P. Cho, K. Oh, K. Ku, I. R. Choi, K. Kang, *Chem. Mater.* **2018**, *30*, 1956–1964.
- [21] W. Zhao, Y. Tsuchiya, N. Yabuuchi, *Small Methods* **2018**, 1800032.
- [22] B. Song, E. Hu, J. Liu, Y. Zhang, X.-Q. Yang, J. Nanda, A. Huq, K. Page, *J. Mater. Chem. A* **2019**, *7*, 1491–1498.
- [23] S. Xu, J. Wu, E. Hu, Q. Li, J. Zhang, Y. Wang, E. Stavitski, L. Jiang, X. Rong, X. Yu, W. Yang, X.-Q. Yang, L. Chen, Y.-S. Hu, *J. Mater. Chem. A* **2018**, *6*, 20795–20803.
- [24] H. R. Yao, P. F. Wang, Y. Gong, J. Zhang, X. Yu, L. Gu, C. OuYang, Y. X. Yin, E. Hu, X. Q. Yang, E. Stavitski, Y. G. Guo, L. J. Wan, *J. Am. Chem. Soc.* **2017**, *139*, 8440–8443.
- [25] Y. Wang, J. Liu, B. Lee, R. Qiao, Z. Yang, S. Xu, X. Yu, L. Gu, Y. S. Hu, W. Yang, K. Kang, H. Li, X. Q. Yang, L. Chen, X. Huang, *Nat. Commun.* **2015**, *6*, 6401.
- [26] K. Zhang, D. Kim, Z. Hu, M. Park, G. Noh, Y. Yang, J. Zhang, V. W. Lau, S. L. Chou, M. Cho, S. Y. Choi, Y. M. Kang, *Nat. Commun.* **2019**, *10*, 5203.
- [27] Y. Xiao, P. F. Wang, Y. X. Yin, Y. F. Zhu, Y. B. Niu, X. D. Zhang, J. Zhang, X. Yu, X. D. Guo, B. H. Zhong, Y. G. Guo, *Adv. Mater.* **2018**, *30*, 1803765.
- [28] J. Li, J. Wang, X. He, L. Zhang, A. Senyshyn, B. Yan, M. Muehlbauer, X. Cao, B. Vortmann-Westhoven, V. Kraft, H. Liu, C. Luerenbaum, G. Schumacher, E. Paillard, M. Winter, J. Li, *J. Power Sources* **2019**, *416*, 184–192.
- [29] S. Doubaji, L. Ma, H. D. Asfaw, I. Izanzar, R. Xu, J. Alami, J. Lu, T. Wu, K. Amine, K. Edstrom, I. Saadoune, *ACS Appl. Mater. Interfaces* **2018**, *10*, 488–501.
- [30] Y. Xie, H. Wang, G. Xu, J. Wang, H. Sheng, Z. Chen, Y. Ren, C.-J. Sun, J. Wen, J. Wang, D. J. Miller, J. Lu, K. Amine, Z.-F. Ma, *Adv. Energy Mater.* **2016**, *6*, 1601306.
- [31] T.-Y. Chen, B. Han, C.-W. Hu, Y.-F. Su, Y.-X. Zhou, H.-Y. Chen, P.-I. Pan, C.-M. Wu, A. Hu, J.-J. Kai, Y.-D. Juang, C.-C. Chang, *J. Phys. Chem. C* **2018**, *122*, 12623–12632.
- [32] L. Mu, X. Feng, R. Kou, Y. Zhang, H. Guo, C. Tian, C.-J. Sun, X.-W. Du, D. Nordlund, H. L. Xin, F. Lin, *Adv. Energy Mater.* **2018**, *8*, 1801975.
- [33] T. Risthaus, D. Zhou, X. Cao, X. He, B. Qiu, J. Wang, L. Zhang, Z. Liu, E. Paillard, G. Schumacher, M. Winter, J. Li, *J. Power Sources* **2018**, *395*, 16–24.
- [34] X. Rong, J. Liu, E. Hu, Y. Liu, Y. Wang, J. Wu, X. Yu, K. Page, Y.-S. Hu, W. Yang, H. Li, X.-Q. Yang, L. Chen, X. Huang, *Joule* **2018**, *2*, 125–140.
- [35] U. Maitra, R. A. House, J. W. Somerville, N. Tapia-Ruiz, J. G. Lozano, N. Guerrini, R. Hao, K. Luo, L. Jin, M. A. Perez-Osorio, F. Massel, D. M. Pickup, S. Ramos, X. Lu, D. E. McNally, A. V. Chadwick, F. Giustino, T. Schmitt, L. C. Duda, M. R. Roberts, P. G. Bruce, *Nat. Chem.* **2018**, *10*, 288–295.
- [36] W. Hua, M. Chen, B. Schwarz, M. Knapp, M. Bruns, J. Barthel, X. Yang, F. Sigel, R. Azmi, A. Senyshyn, A. Missiul, L. Simonelli, M. Etter, S. Wang, X. Mu, A. Fiedler, J. R. Binder, X. Guo, S. Chou, B. Zhong, S. Indris, H. Ehrenberg, *Adv. Energy Mater.* **2019**, *9*, 1803094.
- [37] L. Mu, Q. Hou, Z. Yang, Y. Zhang, M. M. Rahman, D. J. Kautz, E. Sun, X.-W. Du, Y. Du, D. Nordlund, F. Lin, *J. Electrochem. Soc.* **2019**, *166*, A251–A257.
- [38] A. Konarov, J. H. Jo, J. U. Choi, Z. Bakenov, H. Yashiro, J. Kim, S.-T. Myung, *Nano Energy* **2019**, *59*, 197–206.
- [39] J.-J. Ding, Y.-N. Zhou, Q. Sun, Z.-W. Fu, *Electrochim. Commun.* **2012**, *22*, 85–88.
- [40] Y.-N. Zhou, J.-J. Ding, K.-W. Nam, X. Yu, S.-M. Bak, E. Hu, J. Liu, J. Bai, H. Li, Z.-W. Fu, X.-Q. Yang, *J. Mater. Chem. A* **2013**, *1*, 11130–11134.
- [41] M. Cao, T. Wang, Z. Shadike, K. Nam, Y. Zhou, Z. Fu, *J. Electrochem. Soc.* **2018**, *165*, A565–A574.
- [42] J.-H. Cheng, C.-J. Pan, J.-F. Lee, J.-M. Chen, M. Guignard, C. Delmas, D. Carlier, B.-J. Hwang, *Chem. Mater.* **2014**, *26*, 1219–1225.
- [43] W. Olszewski, M. Ávila Pérez, C. Marini, E. Paris, X. Wang, T. Iwao, M. Okubo, A. Yamada, T. Mizokawa, N. L. Saini, L. Simonelli, *J. Phys. Chem. C* **2016**, *120*, 4227–4232.
- [44] M.-H. Cao, Z. Shadike, Y.-N. Zhou, Z.-W. Fu, *Electrochim. Acta* **2019**, *295*, 918–925.
- [45] Q. C. Wang, E. Hu, Y. Pan, N. Xiao, F. Hong, Z. W. Fu, X. J. Wu, S. M. Bak, X. Q. Yang, Y. N. Zhou, *Adv. Sci.* **2017**, *4*, 1700219.
- [46] P. F. Wang, H. Xin, T. T. Zuo, Q. Li, X. Yang, Y. X. Yin, X. Gao, X. Yu, Y. G. Guo, *Angew. Chem. Int. Ed.* **2018**, *57*, 8178–8183.
- [47] Q. Ni, Y. Bai, F. Wu, C. Wu, *Adv. Sci.* **2017**, *4*, 1600275.
- [48] E. Wang, M. Chen, X. Liu, Y. Liu, H. Guo, Z. Wu, W. Xiang, B. Zhong, X. Guo, S. Chou, S.-X. Dou, *Small Methods* **2018**, 1800169.
- [49] Y. S. Yu, M. Farmand, C. Kim, Y. Liu, C. P. Grey, F. C. Strobridge, T. Tyliszczak, R. Celestre, P. Denes, J. Joseph, H. Krishnan, F. Maia, A. L. D. Kilcoyne, S. Marchesini, T. P. C. Leite, T. Warwick, H. Padmore, J. Cabana, D. A. Shapiro, *Nat. Commun.* **2018**, *9*, 921.
- [50] P. Serras, V. Palomares, J. Alonso, N. Sharma, J. M. López del Amo, P. Kubiatk, M. L. Fdez-Gubieda, T. Rojo, *Chem. Mater.* **2013**, *25*, 4917–4925.
- [51] T. Broux, T. Bamine, L. Simonelli, L. Stievano, F. Fauth, M. Ménétrier, D. Carlier, C. Masquelier, L. Croguennec, *J. Phys. Chem. C* **2017**, *121*, 4103–4111.
- [52] B. Wen, Q. Wang, Y. Lin, N. A. Chernova, K. Karki, Y. Chung, F. Omenya, S. Sallis, L. F. J. Piper, S. P. Ong, M. S. Whittingham, *Chem. Mater.* **2016**, *28*, 3159–3170.
- [53] Y. Fang, Q. Liu, L. Xiao, Y. Rong, Y. Liu, Z. Chen, X. Ai, Y. Cao, H. Yang, J. Xie, C. Sun, X. Zhang, B. Aoun, X. Xing, X. Xiao, Y. Ren, *Chem* **2018**, *4*, 1167–1180.
- [54] G. Yan, S. Mariyappan, G. Rousse, Q. Jacquet, M. Deschamps, R. David, B. Mirvax, J. W. Freeland, J. M. Tarascon, *Nat. Commun.* **2019**, *10*, 585.
- [55] D. Wang, X. Bie, Q. Fu, D. Dixon, N. Bramnik, Y. S. Hu, F. Fauth, Y. Wei, H. Ehrenberg, G. Chen, F. Du, *Nat. Commun.* **2017**, *8*, 15888.
- [56] K. H. Kim, J. Choi, S. H. Hong, *Chem. Commun.* **2019**, *55*, 3207–3210.
- [57] J. Ding, Y.-C. Lin, J. Liu, J. Rana, H. Zhang, H. Zhou, I.-H. Chu, K. M. Wiaderek, F. Omenya, N. A. Chernova, K. W. Chapman, L. F. J. Piper, S. P. Ong, M. S. Whittingham, *Adv. Energy Mater.* **2018**, *8*, 1800221.
- [58] S.-M. Bak, R. Qiao, W. Yang, S. Lee, X. Yu, B. Anasori, H. Lee, Y. Gogotsi, X.-Q. Yang, *Adv. Energy Mater.* **2017**, *7*, 1700959.
- [59] Q. Wei, Y. Jiang, X. Qian, L. Zhang, Q. Li, S. Tan, K. Zhao, W. Yang, Q. An, J. Guo, L. Mai, *iScience* **2018**, *6*, 212–221.
- [60] H. Kim, I. Park, S. Lee, H. Kim, K.-Y. Park, Y.-U. Park, H. Kim, J. Kim, H.-D. Lim, W.-S. Yoon, K. Kang, *Chem. Mater.* **2013**, *25*, 3614–3622.
- [61] G. Oyama, O. Pecher, K. J. Griffith, S.-i. Nishimura, R. Pigliapochi, C. P. Grey, A. Yamada, *Chem. Mater.* **2016**, *28*, 5321–5328.
- [62] Y. H. Jung, C. H. Lim, J.-H. Kim, D. K. Kim, *RSC Adv.* **2014**, *4*, 9799–9802.
- [63] W. Huang, J. Zhou, B. Li, J. Ma, S. Tao, D. Xia, W. Chu, Z. Wu, *Sci. Rep.* **2014**, *4*, 4188.
- [64] Y.-N. Zhou, M. Sina, N. Pereira, X. Yu, G. G. Amatucci, X.-Q. Yang, F. Cosandey, K.-W. Nam, *Adv. Funct. Mater.* **2015**, *25*, 696–703.
- [65] L. Wang, J. Song, R. Qiao, L. A. Wray, M. A. Hossain, Y. D. Chuang, W. Yang, Y. Lu, D. Evans, J. Lee, S. Vail, X. Zhao, M. Nishijima, S. Kakimoto, J. B. Goodenough, *J. Am. Chem. Soc.* **2015**, *137*, 2548–2554.
- [66] Y. You, X. Yu, Y. Yin, K.-W. Nam, Y.-G. Guo, *Nano Res.* **2014**, *8*, 117–128.
- [67] A. Mullalui, G. Aquilanti, P. Conti, J. R. Plaisier, M. Fehse, L. Stievano, M. Giorgetti, *J. Phys. Chem. C* **2018**, *122*, 15868–15877.
- [68] A. Firouzi, R. Qiao, S. Motallebi, C. W. Valencia, H. S. Israel, M. Fujimoto, L. A. Wray, Y. D. Chuang, W. Yang, C. D. Wessells, *Nat. Commun.* **2018**, *9*, 861.
- [69] H. Wang, L. Wang, S. Chen, G. Li, J. Quan, E. Xu, L. Song, Y. Jiang, *J. Mater. Chem. A* **2017**, *5*, 3569–3577.
- [70] J. Wu, J. Song, K. Dai, Z. Zhuo, L. A. Wray, G. Liu, Z. X. Shen, R. Zeng, Y. Lu, W. Yang, *J. Am. Chem. Soc.* **2017**, *139*, 18358–18364.
- [71] J. Sottmann, F. L. M. Bernal, K. V. Yusenko, M. Herrmann, H. Emerich, D. S. Wragg, S. Margadonna, *Electrochim. Acta* **2016**, *200*, 305–313.
- [72] J.-H. Lee, G. Ali, D. H. Kim, K. Y. Chung, *Adv. Energy Mater.* **2017**, *7*, 1601491.

- [73] A. Darwiche, M. Fehse, A. Mahmoud, C. L. Fontaine, B. Fraisse, R. P. Hermann, M.-L. Doublet, L. Monconduit, M. T. Sougrati, M. B. Yahia, L. Stievano, *Batteries*. **2018**, *4*, 25.
- [74] M. Fehse, D. Bessas, A. Darwiche, A. Mahmoud, G. Rahamim, C. L. Fontaine, R. P. Hermann, D. Zitoun, L. Monconduit, L. Stievano, Moulay T. Sougrati, *Batteries & Supercaps* **2019**, *2*, 66–73; *Supercaps* **2019**, *2*, 66–73.
- [75] M. Fehse, A. Ladecola, M. T. Sougrati, P. Conti, M. Giorgetti, L. Stievano, *Energy Storage Mater.* **2019**, *18*, 328–337.
- [76] Y. Tsuchiya, K. Takanashi, T. Nishinobu, A. Hokura, M. Yonemura, T. Matsukawa, T. Ishigaki, K. Yamanaka, T. Ohta, N. Yabuuchi, *Chem. Mater.* **2016**, *28*, 7006–7016.
- [77] M. Chen, W. Hua, J. Xiao, D. Cortie, W. Chen, E. Wang, Z. Hu, Q. Gu, X.-L. Wang, S. Idris, S.-L. Chou, S.-X. Dou, *Nat. Commun.* **2019**, *10*, 1480.
- [78] M. Chen, E. Wang, Q. Liu, X. Guo, W. Chen, S.-L. Chou, S.-X. Dou, *Energy Storage Mater.* **2019**, *19*, 163–178.

Manuscript received: April 10, 2019

Revised manuscript received: June 14, 2019

Accepted manuscript online: June 17, 2019

Version of record online: July 11, 2019
